Additive Manufacturing 59 (2022) 103068

Contents lists available at ScienceDirect

Additive Manufacturing

journal homepage: www.elsevier.com/locate/addma

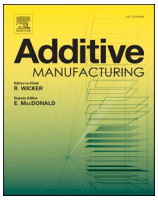

Phase transformation dynamics guided alloy development for additive manufacturing

Qilin Guo [a,b], Minglei Qu [a,b], Chihpin Andrew Chuang [c], Lianghua Xiong [d], Ali Nabaa [a,b], Zachary A. Young [a], Yang Ren [c], Peter Kenesei [c], Fan Zhang [e,*], Lianyi Chen [a,b,**]

[a] Department of Mechanical Engineering, University of Wisconsin–Madison, Madison, WI 53706, USA
[b] Department of Materials Science and Engineering, University of Wisconsin–Madison, Madison, WI 53706, USA
[c] X-ray Science Division, Argonne National Laboratory, Lemont, IL 60439, USA
[d] Department of Mechanical and Aerospace Engineering, Missouri University of Science and Technology, Rolla, MO 65409, USA
[e] Materials Measurement Science Division, National Institute of Standards and Technology, Gaithersburg, MD 20899, USA

ARTICLE INFO

Keywords:
Additive manufacturing
Laser processing
Phase transformation
Synchrotron X-ray diffraction
17–4 PH stainless steel

ABSTRACT

Fusion-based additive manufacturing technologies enable the fabrication of geometrically and compositionally complex parts unachievable by conventional manufacturing methods. However, the non-uniform and far-from-equilibrium heating/cooling conditions pose a significant challenge to consistently obtaining desirable phases in the as-printed parts. Here we report a martensite stainless steel development guided by phase transformation dynamics revealed by in-situ high-speed, high-energy, high-resolution X-ray diffraction. This developed stainless steel consistently forms desired fully martensitic structure across a wide range of cooling rates (10^2–10^7 °C/s), which enables direct printing of parts with fully martensitic structure. The as-printed material exhibits a yield strength of 1157 ± 23 MPa, comparable to its wrought counterpart after precipitation-hardening heat-treatment. The as-printed property is attributed to the fully martensitic structure and the fine precipitates formed during the intrinsic heat treatment in additive manufacturing. The phase transformation dynamics guided alloy development strategy demonstrated here opens the path for developing reliable, high-performance alloys specific for additive manufacturing.

1. Introduction

Fusion-based additive manufacturing (AM), e.g., laser powder bed fusion (LPBF), directed energy deposition (DED), integrates material synthesis and part manufacturing into a single step. It has the potential to revolutionize the manufacturing industry by enabling customized production of geometrically and compositionally complex parts with unprecedented functionality and performance [1,2].

However, the complex and often extreme thermal conditions of AM, intrinsic to a localized heat source-material interaction, pose considerable challenges to consistently obtaining desired phases in the as-printed parts, especially for materials with multi-stage phase transformations during AM fabrication (e.g., steel [3], titanium alloy [4], nickel superalloy [5,6]). These challenges frequently manifest themselves in three aspects: (1) AM solidification occurs far from equilibrium due to its rapid cooling rate, causing the phase transformation sequence/timing to deviate from predictions made by equilibrium phase diagram [7,8]. (2) The heating/cooling conditions at different locations of the melt pool are heterogeneous, leading to diversified phase constitutions within a single melt pool [9,10]. (3) The thermal conditions across different machines, across different parts within the same batch, and even across different regions within a single part are all different, leading to inconsistent phase constitutions from print to print [11].

One prominent example is 17–4 precipitation-hardening (PH) martensitic stainless steel (also known as 17–4 PH or type 630 stainless steel), which exhibits various unwanted phases in the AM as-printed condition [12]. In conventional manufacturing process with low cooling rate, 17–4 PH steel solidifies following a phase transformation sequence of liquid (L)–δ-ferrite (δ)–austenite (γ)–martensite (α') [13]. δ-ferrite (δ) and martensite (α') in 17–4 have a body-centered cubic (BCC) lattice structure, while austenite (γ) has a face-centered cubic (FCC) lattice structure. The desired final phase in 17–4 PH steel is the

* Corresponding author.
** Corresponding author at: Department of Mechanical Engineering, University of Wisconsin–Madison, Madison, WI 53706, USA.
E-mail addresses: fan.zhang@nist.gov (F. Zhang), lianyi.chen@wisc.edu (L. Chen).

https://doi.org/10.1016/j.addma.2022.103068
Received 19 May 2022; Received in revised form 13 July 2022; Accepted 29 July 2022
Available online 2 August 2022

martensitic phase (α'), enabling its excellent mechanical performance. The typical processing of 17–4 steel also includes a high-temperature solution heat treatment, followed by quenching and aging at low temperatures for an extended period to introduce nanoscopic precipitates, which further increases its mechanical strength. In general, precipitation-hardening (PH) stainless steels have the highest tensile strength of stainless steels. 17–4 steel is the most widely used PH grade stainless steel and has drawn much attention for its potential applications enabled by AM technologies.

However, the development of AM 17–4 steel has encountered severe phase control challenges. While martensite in conventional 17–4 provides its primary strength, AM 17–4 in its as-built state can contain a significant amount of retained austenite (up to 100 % reported in literature) and even a large fraction of δ-ferrite (up to >95 % reported in literature) [14–25]. To make things worse, the fractions of residual austenite and δ-ferrite phases also vary significantly across different

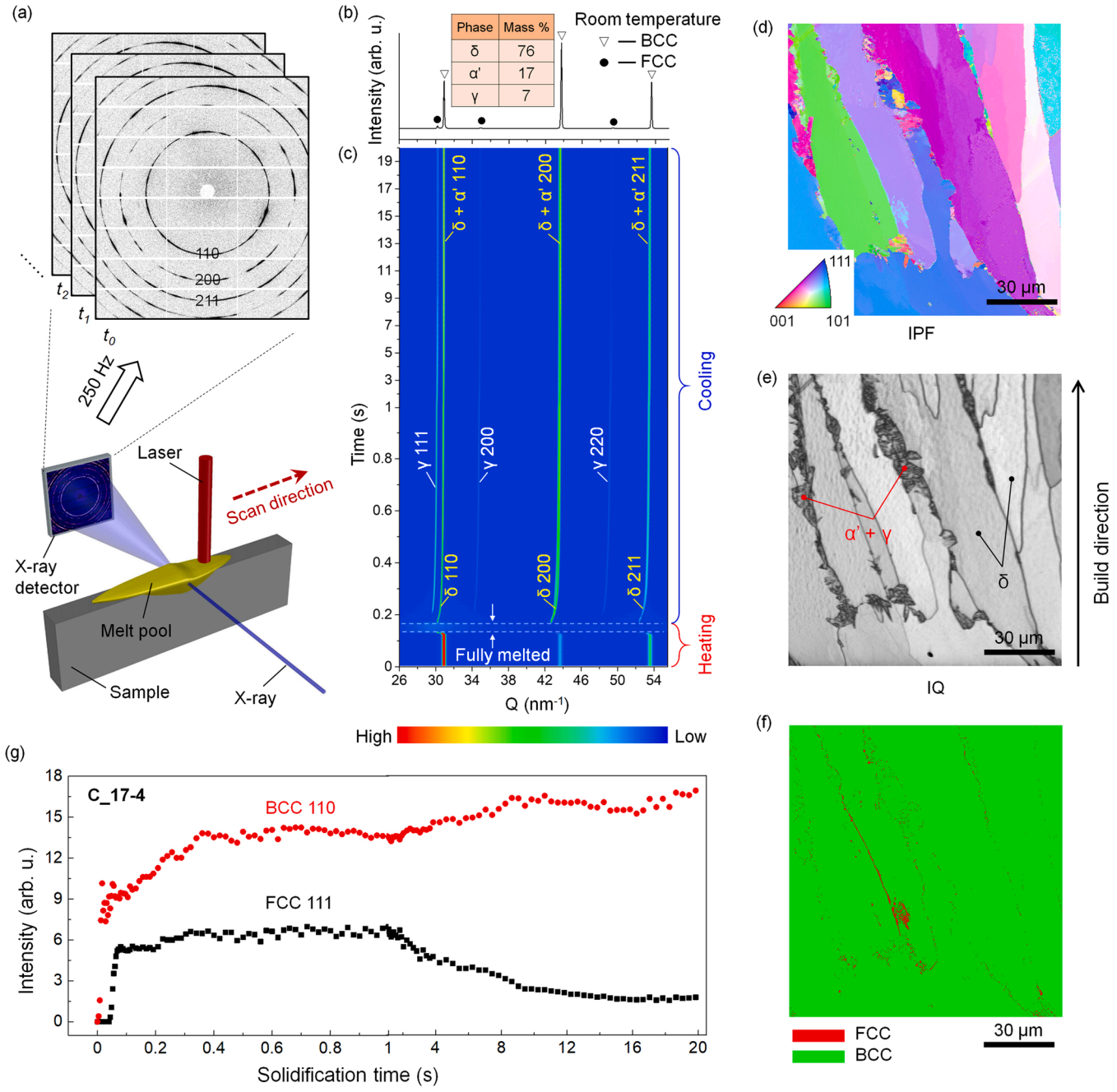

Fig. 1. Characterization of phase transformation dynamics of commercial additively manufactured 17–4 stainless steel (C_17–4) during laser melting. (a) Schematic illustration of in-situ laser-melting X-ray diffraction experiment. A vertical laser beam scans the sample to create a localized melt pool. The micro-focused high-energy X-ray beam is used to probe the phase transformation dynamics with a frame rate of 250 Hz. (b) Room temperature XRD pattern of as-solidified C_17–4 after laser melting. (c) XRD intensity map (XRD peak intensity evolution as a function of time) during laser melting of C_17–4 from 0 s to 20 s. The liquid gap near 0.15 s without any diffraction peaks denotes the period when all the material in the X-ray path was fully melted. The time axis is enlarged in the 0–1 s range to highlight the phase transformation details during the initial solidification stage. (d) EBSD of as-printed C_17–4 microstructure displayed in inversed pole figure (IPF) coloring. (e) EBSD of as-printed C_17–4 microstructure displayed in image quality (IQ) map. Martensite (α') phase and a mixture of austenite (γ) and δ-ferrite (δ) phases were pointed out in the microstructure. (f) EBSD phase map of as-printed C_17–4. (g) XRD intensity evolution from (c) during solidification. The time axis is enlarged in the 0–1 s range. The uncertainty for BCC intensity measurement is 1 %. The uncertainty for FCC intensity measurement is 2 %.

printing parameters, AM build machines, and AM technologies. These residual phases deteriorate the properties of the printed parts and create significant uncertainties in the targeted applications that rely on the designed properties of 17–4 steels [18,22,26–28]. It is, therefore, imperative to understand the nonequilibrium phase transformation sequence of 17–4 steel during AM processing and develop an alloy within the 17–4 composition window that can reproducibly deliver 17–4′s performance characteristics desirably in its as-built state.

Here, we report the development of a 17–4 PH martensitic stainless steel with formation of a fully martensitic microstructure across a broad range of cooling rates (10^2–10^7 ℃/s), guided by the phase transformation dynamics revealed by in-situ high-speed, high-energy, high-resolution synchrotron X-ray diffraction (XRD). The phase transformation dynamics results guided our alloy development to focus on the liquid-solid phase transformation during initial solidification, in contrast to the common strategy mainly focusing on the solid-solid phase transformation. This designed alloy demonstrates great tolerance to cooling rate variation, thus overcoming the three challenges mentioned earlier. It also takes advantage of the intrinsic heat treatment of AM processing to form strengthening precipitates in its as-printed condition. Its combination of fully martensitic structure and fine precipitates leads this alloy to have good mechanical properties, following one-step processing.

2. Experimental procedures

2.1. In-situ laser melting synchrotron X-ray diffraction experiment

We used in-situ laser-melting X-ray diffraction (XRD) experiment to probe the phase transformation dynamics in 17–4 PH stainless steel. The experiment was conducted at the beamline 1-ID-E of the Advanced Photon Source (APS), Argonne National Laboratory. The setup was described in details in references [29,30]. The configuration of the laser beam, the X-ray beam, and the sample positioning is schematically shown in Fig. 1(a). During the experiment, the sample was placed in a vacuum chamber refilled with argon for protection. A continuous-wave single-mode ytterbium fiber laser (model YLR-500-AC, IPG Photonics, USA) controlled by a galvo scanner (IntelliSCAN$_{de}$ 30, SCANLAB GmbH, Germany) was used to perform laser scanning and melting on the samples. The maximum laser output power was 560 W with a wavelength of 1070 nm. The $1/e^2$ laser beam size was ~100 μm. Laser scan speed varied from 0.05 m/s to 1.0 m/s to achieve different cooling rates.

During laser scanning, a stationary micro-focused high-energy high-flux synchrotron X-ray beam with a wavelength of 0.2022 Å and a beam size of 50 μm × 30 μm (horizontal × vertical) was transmitted through the sample (0.5 mm thick) to form Debye-Scherrer diffraction cones, which were continuously recorded as diffraction rings on a flat plate detector (PILATUS3X-2 M, DECTRIS, Switzerland) with a recording frame rate of 250 Hz. The X-ray exposure time for every frame is 1 ms. The synchrotron X-ray's high brilliance and high energy (short wavelength) properties ensured the XRD data with a high signal-to-noise ratio and a broad $\boldsymbol{Q}$-space range (covering more families of crystallographic planes) [48,49]. They also enabled quantitative analysis of the bulk structural information of the specimen and prevents uncertainties introduced by surface effect (deformation-induced γ–α' transformation) from sample preparation [14].

2.2. XRD peak analysis

The diffraction rings from each frame were radially integrated by FIT2D software along the entire azimuthal range (0–360°) to obtain intensity versus $\boldsymbol{Q}$-vector patterns. Here, $|\boldsymbol{Q}| = 4\pi \times \sin(\theta)/\lambda$, where λ is the X-ray wavelength and θ is one half of the diffraction angle 2θ. Each integrated pattern contains 2048 bins in a $|\boldsymbol{Q}|$ range of 26 nm^{-1} to 55.5 nm^{-1}. The peak position and peak intensity were determined by a Voigt function. An example of the integrated XRD pattern is shown in Fig. 1(b), revealing the room-temperature phase constitution of commercial additively manufactured 17–4 PH stainless steel (hereinafter, C_17–4) after laser melting.

2.3. Estimation of phase fraction

Rietveld refinement was performed by GSAS-II software to determine the phase fraction from XRD patterns. The reference phase information was obtained from Inorganic Crystal Structure Database (ICSD) with IDs of ICSD-53449 (austenite), ICSD-53452 (delta-ferrite), and ICSD-53451 (alpha-ferrite). A standard CeO_2 powder specimen was used to calibrate the experiment configuration. The background, scale factor, lattice constants, grain size, and microstrain were all considered in the refinement.

2.4. Determination of lattice parameter-temperature relationship

In-situ furnace heating/cooling X-ray diffraction experiments were conducted at the APS beamline 11-ID-C by heating a sample in a Linkam TS1500 Heating Stage (Linkam Scientific Instruments) with heating/cooling rate set to 20 ℃/min within a temperature range of 50–1100 ℃. XRD patterns were acquired every 50 ℃. Lattice parameters above 1100 ℃ was obtained by a linear extrapolation. Thermomechanical analysis (TMA) was performed on NETZSCH TMA 402 F1, following the ASTM E831-19 standard. The heating/cooling rate was set to 20 ℃/min within a temperature range of 50–1000 ℃. Both experiments were shielded by high-purity argon gas (99.999 %).

2.5. Tensile test

Tensile tests were performed on an MTS Criterion 40 electromechanical universal test system (Model 43). The strain rate was 2.5×10^{-4} s^{-1}. The geometry and dimensions of the specimens follow the tensile specimen design (MT2) developed for additively manufactured metals reported in reference [31]. All specimens were cut by wire electrical discharge machining (EDM) followed by surface grinding to 1200 grit (5 μm).

2.6. Small-angle X-ray scattering (SAXS) experiment

We performed small-angle X-ray scattering (SAXS) measurement at the APS ultra-small-angle X-ray scattering beamline 9-ID-C to determine the nanoscopic microstructural features in the as-printed 17–4 steel. Because of its Bonse-Hart crystal optics, this instrument provides primary intensity calibration, enabling analysis of absolute volume fraction of scattering inhomogeneities [32]. We used a standard configuration of this instrument to acquire ultra-small-angle X-ray scattering and X-ray diffraction data of the same sample volume across a broad $|\boldsymbol{Q}|$ range from 1×10^{-4} $Å^{-1}$ to 6.5 $Å^{-1}$ [33]. A detailed description of this setup can be found in reference [34]. The X-ray energy was 21 keV, corresponding to an X-ray wavelength of 0.5904 Å. We carefully polished a thin foil of as-built 17-4 steel with a thickness of ~100 μm (transmission of ~14 %) to ensure penetration. We analyzed the data using standard small angle scattering analysis software Irena [35].

2.7. Materials

The commercial additively manufactured 17–4 PH stainless steel (C_17–4) specimens for in-situ XRD experiments and tensile testing were fabricated by a laser powder-bed fusion machine with commercial feedstock powder (argon-atomized). The chemical composition was mainly analyzed by inductively coupled plasma (ICP) analysis, except that the C and S were analyzed by combustion method while O and N were quantified by inert gas fusion. The detailed composition is shown in Table 1. The C_17–4 samples are in the as-printed state without any post-build heat treatment.

Table 1
Chemical composition (mass %) of 17–4 PH stainless steel.

Element	Specification	C_17–4	UW_17–4 (Nominal)	UW_17–4 (Arc-melt)	UW_17–4 (Atomized)	UW_17–4 (As-printed)
Cr	15.0–17.5	16.7 ± 0.84	15.2	15.29 ± 0.76	15.53 ± 0.78	15.72 ± 0.31
Ni	3.0–5.0	4.3 ± 0.43	4.8	4.78 ± 0.48	4.92 ± 0.49	4.84 ± 0.24
Cu	3.0–5.0	4.0 ± 0.4	5.0	4.91 ± 0.49	4.99 ± 0.50	4.91 ± 0.25
Mn	1.0 max.	0.22 ± 0.02	–	< 0.001 ± 0.0003	0.012 ± 0.003	0.011 ± 0.002
Nb	0.15–0.45	0.3 ± 0.03	0.3	0.311 ± 0.031	0.42 ± 0.11	0.27 ± 0.04
C	0.07 max.	0.02 ± 0.005	–	0.002 ± 0.0005	0.001 ± 0.0003	0.006 ± 0.001
N	–	0.027 ± 0.007	–	0.005 ± 0.001	0.001 ± 0.0003	0.001 ± 0.0002
O	–	0.058 ± 0.015	–	0.019 ± 0.005	0.022 ± 0.006	0.034 ± 0.005
Si	1.0 max.	0.34 ± 0.03	–	0.009 ± 0.002	< 0.001 ± 0.0003	0.01 ± 0.002
S	0.03 max.	0.003 ± 0.0008	–	0.002 ± 0.0005	0.002 ± 0.0005	0.003 ± 0.0005
P	0.04 max.	0.011 ± 0.003	–	0.007 ± 0.002	< 0.001 ± 0.0003	< 0.005 ± 0.001
Fe	Bal.	Bal.	Bal.	Bal.	Bal.	Bal.

Our developed alloy (hereinafter, UW_17–4) for in-situ XRD experiments was cast in an arc melter (model SP-MSM20–8, MTI Corporation, USA) with metal elements pre-weighed by a high-precision balance (model PA224C, OHAUS Corporation, USA) with an accuracy of 0.0001 g. The purity of base elements is 99.98 % for Fe, 99.995 % for Cr, 99.995 % for Ni, 99.995 % for Cu, and 99.97 % for Nb. The arc melting current was 185 A with a melting duration of 15–25 s until the material was fully melted. The ingots were flipped and re-melted six times to ensure composition uniformity. The cast ingots went through a condition-A solution heat treatment (heating rate 12 ℃/min, holding at 1038 ± 5 ℃ for 45 min) in a KSL-1500 Muffle Furnace (MTI Corporation, USA) followed by a water quench. The final phase after quenching was fully martensitic (confirmed by synchrotron XRD and electron backscatter diffraction (EBSD)).

The as-printed UW_17–4 part was made in a powder bed fusion system under high-purity argon environment (> 99.999 %). The feedstock powder was argon-atomized in Arcast HELGA system (Arcast Inc., USA) using as-cast ingots. The laser power was 520 W with a nominal D4σ beam size of ~170 μm, a wavelength of 1070 nm, and a scan hatch spacing of 80 μm. The chemical composition of UW_17–4 at different fabrication stages (arc-melt, atomization, LPBF) were characterized by a combination of ICP analysis, combustion method (for C and S), and inert gas fusion method (for O and N). The results are displayed in Table 1.

The wrought 17–4 PH steel was purchased from McMaster-Carr in an annealed state. Condition-A solution heat treatment (1038 ± 5 ℃ for 45 min) was performed for the tensile testing specimens.

2.8. Electron microscopy

Scanning electron microscopy (SEM) and electron backscatter diffraction (EBSD) were performed on a Zeiss LEO-1530 field emission scanning electron microscope. The samples were mechanically polished with 0.05 μm diamond suspension followed by ion milling (Leica EM TIC 3X). For SEM observation of metallurgical pores, the ion milling was conducted with 3 kV, 1.5 mA at a milling angle of 30° for 3 min. For EBSD purpose, the samples were ion milled with 3 kV, 1.8 mA at a milling angle of 4.5° for 1 h. The EBSD was performed under a 30 kV accelerating voltage with a step size of 0.2–1 μm.

2.9. Atom probe tomography

The needle-shaped specimen for atom probe tomography (APT) test was prepared by focused ion beam (FIB) milling (FEI Helios Nanolab SEM/FIB). Prior to FIB milling, the sample surface was polished following the EBSD specimen preparation procedure, as detailed in the section 2.8. APT test was conducted on a CAMECA LEAP 5000 XS with a 355 nm wavelength ultraviolet laser. The test was run under ultra-high vacuum at $\sim 2 \times 10^{-11}$ torr. The tip base temperature was set to 50 K. The laser pulse energy was 20 pJ, with a pulse frequency of 250 kHz. The detection rate was 2.0–4.0 % of the laser pulse frequency. The run stopped after 60 M detection events at 7.4 kV applied voltage.

3. Results

3.1. In-situ characterization of phase transformation dynamics

To visualize the phase transformation dynamics in C_17–4 during laser melting, the integrated XRD patterns were organized as a function of time to form an XRD intensity map, as shown in Fig. 1(c). The time axis is magnified between 0 and 1 s to highlight the structural transformation details during laser melting. The evolution of XRD intensities includes two stages: (1) a heating stage when the moving laser approached the X-ray-illuminated area and then completely melted the material in the X-ray path, and (2) a cooling stage when the laser moved away while the material started to solidify and cool down. During solidification, Fig. 1(c) indicates that the δ-ferrite (δ) phase emerged first from the liquid, followed by the formation of austenite (γ). In conventional manufacturing with a slow cooling rate, a complete phase transformation of δ–γ and then γ–α' was expected, resulting in a final microstructure dominated by martensite (α'). However, during laser melting of C_17–4, neither of these two transformations completed, as indicated by the continuous δ peaks in the intensity map (Fig. 1(c)) and the presence of FCC diffraction peaks in the room-temperature XRD (Fig. 1(b)). As a result, the final microstructure in laser melted C_17–4 is dominated by coarse δ-ferrite grains developed epitaxially along the building direction, as shown by Fig. 1(d–f). Small amount of mixed martensite grains and austenite grains were observed along the δ-ferrite grain boundaries.

To further confirm that the initially solidified δ-ferrite can survive into final structure at room temperature, we examined the 2D in-situ XRD patterns associated with Fig. 1(c) to analyze the development of δ-ferrite during laser melting of C_17–4. The 2D diffraction patterns/rings at representative moments from initial solidification to room temperature are displayed in Fig. 2. (Fig. 2 and Fig. 1(c) share the same time scale.) The horizontal and vertical black bands in the figures are no-signal zones, due to the configuration of the X-ray detector. At 0.188 s, Fig. 2(a) shows the diffraction pattern at initial solidification, where only δ-ferrite was just formed from the liquid. Since the δ-ferrite grains are large (as shown in Fig. 1(d–f)) and the number of grains along the X-ray path is small, the diffraction pattern appears scattered. Two representative diffraction areas 1 and 2 were enlarged to clearly show the diffraction spots from several δ-ferrite grains. During cooling, austenite was formed, as indicated by the γ 111 diffraction pattern in Fig. 2(b and c). The formation of austenite did not have significant influence on the brightness of δ-ferrite diffraction spots. When temperature went below the martensite start temperature (Ms), martensite started to form, as indicated by the ribbons overlapping with the δ-ferrite diffraction spots in Fig. 2(d). Since martensite structure is fine and rather randomly oriented, its 2D diffraction pattern appears to be a ring/ribbon rather than scattered spots. When the material cooled down to room temperature (Fig. 2(e)), the diffraction pattern exhibited a mixture of three phases: martensite (as indicated by the α' 110 and 200 diffraction ribbons), austenite (as indicated by the γ 111 diffraction ribbon), and δ-ferrite (as

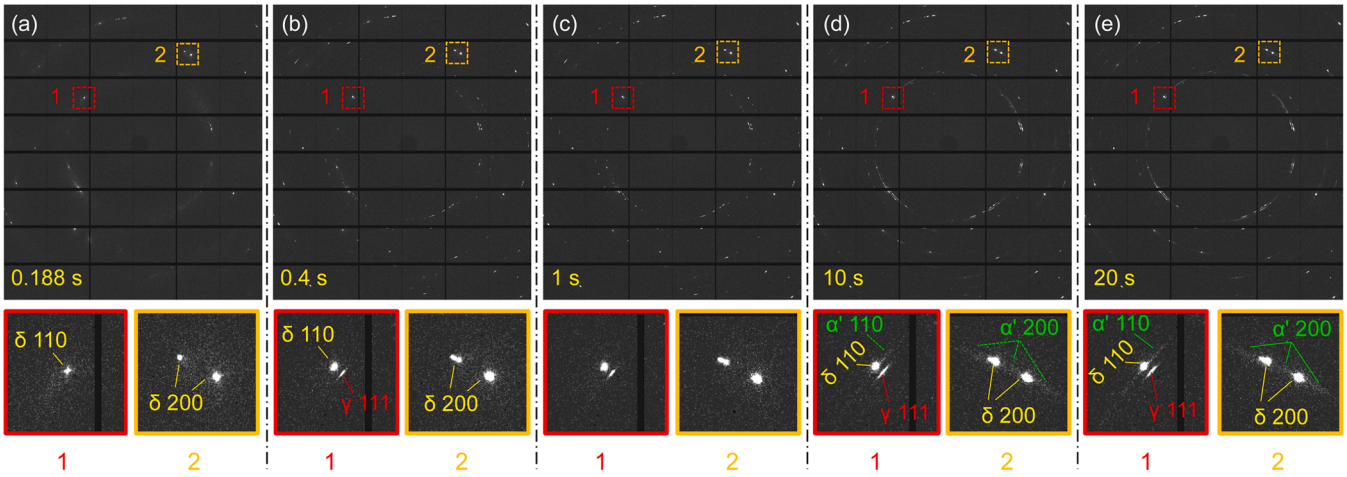

Fig. 2. Phase transformation dynamics in C_17–4 after laser melting. The 2D diffraction patterns at different moments from Fig. 1(c) are shown in (a–e). Fig. 2 and Fig. 1(c) share the same time scale. Two signature diffraction areas 1 and 2 were marked using red and orange lines. The areas 1 and 2 at each moment were enlarged and displayed below the whole-field diffraction images. The horizontal and vertical black bands in the figures are no-signal zones, due to the configuration of the X-ray detector.

indicated by the δ 110 and 200 diffraction spots retained from the initial solidification). Please refer to Supplementary Fig. 1 for the analysis of more δ-ferrite diffraction spots.

To estimate the final phase constitution of C_17–4 after laser melting, we used a Rietveld refinement analysis following two steps. We first determined the FCC and BCC phase fraction at 0.6 s from Fig. 1(c). At this moment, both δ-ferrite and austenite were fully developed (as indicated by the plateau of peak intensity–time curve in Fig. 1(g)), yet the austenite-to-martensite transformation has not started (validated from the 2D diffraction pattern). Therefore, the BCC diffraction at this moment solely came from the residual δ-ferrite and will retain to room temperature. We then determined the FCC and BCC phase fraction at room temperature. The additional fraction of BCC phase at room temperature compared to the BCC fraction at 0.6 s was attributed to the martensite formed from γ–α' transformation. It should be noted that the phase fraction analysis from Rietveld refinement was based on powder diffraction. The discrete diffraction spots of δ-ferrite added to the uncertainty of the phase fraction estimation. Therefore, the analysis here is rather qualitative than quantitative. Hence, we estimated that the final phase constitution in laser-melted C_17–4 contains 76 mass % residual δ-ferrite, 7 mass % residual austenite, and only 17 mass % desired martensite.

For the first time, we directly and unambiguously demonstrated the existence of a substantial amount of δ-ferrite in the as-printed 17–4 PH steel. Due to the low carbon content in the 17–4 stainless steel, the tetragonal distortion of the BCC structure induced by martensite transformation cannot be detected from 1D XRD patterns, resulting in a difficulty of distinguishing δ-ferrite and martensite in the as-printed part. The direct observation of the phase evolution from 2D diffraction patterns by our in-situ experiment provides definitive conclusion.

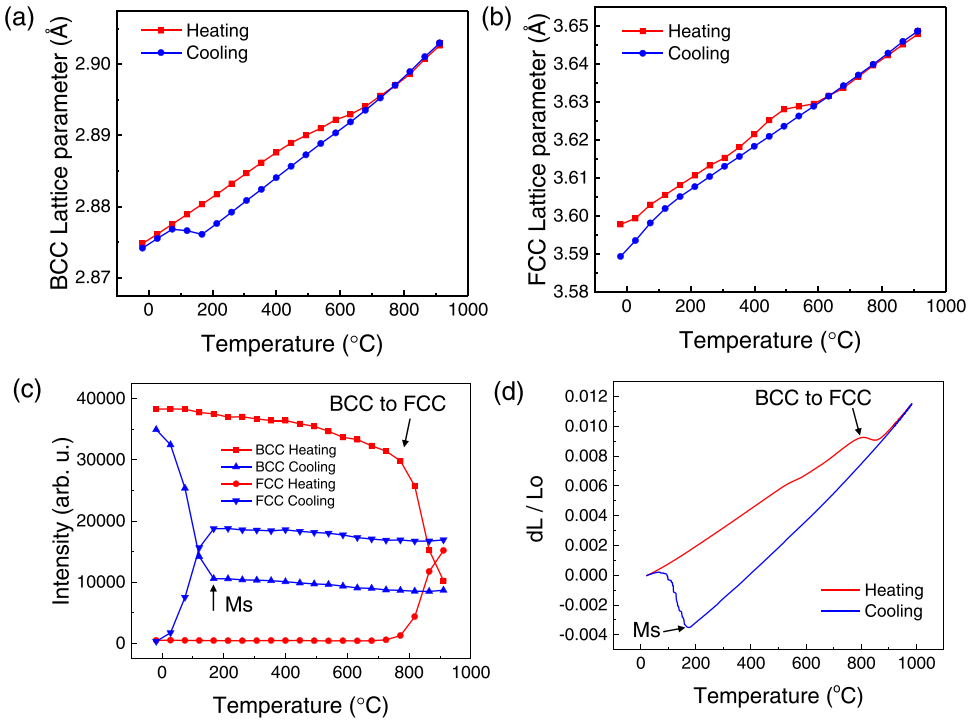

Fig. 3. Determination of temperature-dependent lattice parameters in C_17–4. (a) BCC lattice parameter change measured by in-situ furnace heating-cooling XRD test. (b) FCC lattice parameter change during in-situ furnace heating-cooling XRD test. (c) BCC and FCC diffraction peak intensity change as a function of temperature during in-situ furnace heating-cooling XRD test. (d) Thermomechanical analysis (TMA) test showing the dilation as a function of temperature. The material is C_17–4. The heating/cooling rate was set to 20 °C/min for all tests. The uncertainty for lattice parameter measurements in (a) and (b) is 0.0002 Å. The uncertainty for intensity measurement in (c) is 0.4 %. The uncertainty for thermal expansion measurement in (d) is 2 %.

The cooling rate in our laser-melting experiment during the initial solidification was estimated based on the thermal-expansion-induced change in lattice parameters. We measured the temperature (T) dependent lattice parameter (a) by an in-situ furnace heating/cooling XRD experiment performed at the APD beamline 11-ID-C. Fig. 3(a and b) show the constructed a–T relationship of BCC and FCC phases during heating and cooling of C_17–4, respectively. In addition, the intensity-versus-temperature curves in Fig. 3(c) indicate the phase transformation events during the thermal process. We further calibrated the temperatures using thermomechanical analysis (TMA) on C_17–4 (Fig. 3(d)) by assigning the martensite start temperature (Ms) and BCC–FCC transition temperature measured from the TMA test (Fig. 3(d)) to the corresponding events denoted by X-ray intensity evolutions from in-situ testing (Fig. 3(c)). With the calibrated a–T relationship, we estimated the cooling rate during the initial solidification of C_17–4 in Fig. 1(c) to be 1.7×10^4 ℃/s by evaluating the lattice parameter change within a certain period (da/dt). To be noted, all the cooling rates in this paper refer to the initial solidification cooling rate measured based on the diffraction peak shift in the solid phase within a 50 μm × 30 μm sampling area under 250 Hz recording frame rate (1 ms X-ray exposure for each frame).

3.2. Phase transformation dynamics guided alloy development based on phase fraction during initial solidification

Under the cooling rate of 1.7×10^4 ℃/s, we observed a highly stabilized δ-ferrite that sustained to room temperature, as indicated by Fig. 2 as well as the quantified XRD intensity evolution as a function of time in Fig. 1(g). Previous studies reported that a high cooling rate of 10^5–10^6 ℃/s is required to bypass the δ–γ transformation in 17–4 PH steel due to the insufficient time (up to ~6 ms) spent within the δ–γ transformation temperature range (roughly from 600−800 ℃ to 1250–1450 ℃, depending on specific compositions) [7,16,36–38]. However, our experiment, conducted under a lower cooling rate on the order of 10^4 ℃/s, extended the time spent in the δ–γ transformation range by tenfold (on the order of ~60 ms). Yet, the δ–γ transformation still did not occur, suggesting that the initially solidified δ-ferrite is highly stable.

Previous alloy development work focused on tuning the solid-solid phase transformation (δ–γ) to obtain more martensite in the final 17–4 structure [37]. The strategy was to increase the austenite stabilizing temperature range, so that the δ–γ transformation could have more time to complete during solidification, which leaves more austenite available to transform into martensite. However, our results suggest that the initially solidified δ-ferrite can be too stable to efficiently transform into austenite, even with extended time spent during δ–γ transformation.

In light of such findings, we developed a different alloy development strategy by targeting the liquid-solid phase transformation (liquid–δ), instead of the solid-solid phase transformation (δ–γ). Specifically, the goal is to minimize the formation of δ-ferrite during initial solidification. By decreasing the initially solidified δ-ferrite, more austenite will form during initial solidification. Next, to facilitate the austenite-to-martensite transformation, we removed several minor alloying elements from the alloy composition, including C, Mn, and Si, as they are known to reduce the Ms temperature and delay the γ–α' transformation [39,40]. As a result of the two-step design, more martensite could be obtained in the final as-solidified 17–4 structure.

To minimize initially solidified δ-ferrite, we first investigated the individual effects of three major alloying elements (Cr, Ni, Cu) on the maximum solidified δ-ferrite fraction during equilibrium solidification using the CALPHAD (Calculation of Phase Diagrams) method, with the assumption that phase evolution under equilibrium condition may provide some guidance to our alloy development for rapid cooling conditions. The calculation included all the major alloying elements (Cr, Ni, Cu) and necessary element (Nb) from the 17–4 specification. When varying the concentration of a specific alloying element, the rest alloying elements were kept constant at the median of the 17–4 specification: Cr-16.3 %, Ni-4 %, Cu-4 %, Nb-0.3 %. The calculation results (in Supplementary Fig. 2) suggest that, to obtain less δ-ferrite during initial solidification, it is necessary to reduce the Cr concentration while increase the Ni and Cu concentration in the alloy.

To check whether the CALPHAD calculation results can provide any indication on the phase transformation trend under rapid cooling conditions, we developed an alloy composition with low Cr but high Ni and Cu within the specification to examine the real phase transformation dynamics during laser melting via in-situ laser melting XRD experiments. The nominal alloy composition is $Fe_{74.7}Cr_{15.2}Ni_{4.8}Cu_{5.0}Nb_{0.3}$ (UW_17–4), fabricated by arc melting. During alloy development, the following strategies were taken into consideration:

1. Only major alloying elements (Cr, Ni, Cu) and necessary elements (Nb) were included in the alloy, while the minor elements (C, Mn, Si, S, P) were excluded, for several reasons: (I) C, Mn, and Si can reduce the Ms temperature. They were removed to promote a complete austenite-to-martensite transformation and avoid having residual austenite in the final structure. (II) Minor elements are mostly volatile elements (Mn, Si, S, P) during laser processing, which increases the risk of introducing porosity into the part during laser metal additive manufacturing [41]. (III) The minor elements are allowed to be zero from the 17–4 specification. The newly developed alloy can still be classified as 17–4 stainless steel, without the need to go through additional certification process. (IV) Excluding the minor elements simplifies the alloy fabrication process, as it is difficult to accurately maintain the concentration of minor elements. The uncertain concentration of minor elements also poses challenges for evaluating the effects of major elements on the phase transformation dynamics.
2. Cr and Ni fractions were close to but not exactly at the limit of the specification, to accommodate the concentration fluctuations during fabrication.
3. The fraction of Cu was set to 5 % (maximum allowable concentration in 17–4 specification) for all compositions, for two reasons: (I) More Cu can potentially reduce the stability of initially solidified δ-ferrite, as suggested by Supplementary Fig. 2(c). (II) More Cu can potentially promote Cu precipitate formation during intrinsic heat treatment caused by the layer-by-layer repetitive thermal cycling [22], if the alloy is going to be processed via additive manufacturing.

The actual UW_17–4 alloy compositions during each processing step were tested by a combination of ICP analysis, combustion method (for C and S), and inert gas fusion method (for O and N). The results are displayed in Table 1.

To confirm the UW_17–4 favors the formation of martensite by reducing the amount of initially solidified δ-ferrite (increasing the amount of austenite from initial solidification), we examined its phase transformation dynamics during laser processing from both the XRD intensity map (Fig. 4(b)) and the 2D diffraction patterns (Fig. 5). The XRD intensity map in Fig. 4(b) was converted from the same set of 2D patterns as in Fig. 5. Fig. 4(b) and Fig. 5 share the same time scale.

From the XRD intensity map in Fig. 4(a–c), δ-ferrite is still the first phase formed from the liquid under a cooling rate of 1.7×10^4 ℃/s. Soon, the short-lived δ-ferrite transformed into austenite completely, as indicated in Fig. 4(c). In contrast to C_17–4, no δ-ferrite peaks sustained into the austenite regime, suggesting reduced stability of the δ-ferrite in UW_17–4 compared with that of C_17–4. Subsequently, the fully austenite structure started to transform into martensite at lower temperature ($t \approx 1.5$ s, Fig. 4(b)). The austenite-to-martensite transformation completed before reaching room temperature, leaving a fully martensitic as-solidified structure, as evidenced by the room-temperature XRD pattern in Fig. 4(a).

The 2D diffraction patterns in Fig. 5 presented the same story from another perspective. During initial solidification (0.172 s), δ-ferrite first

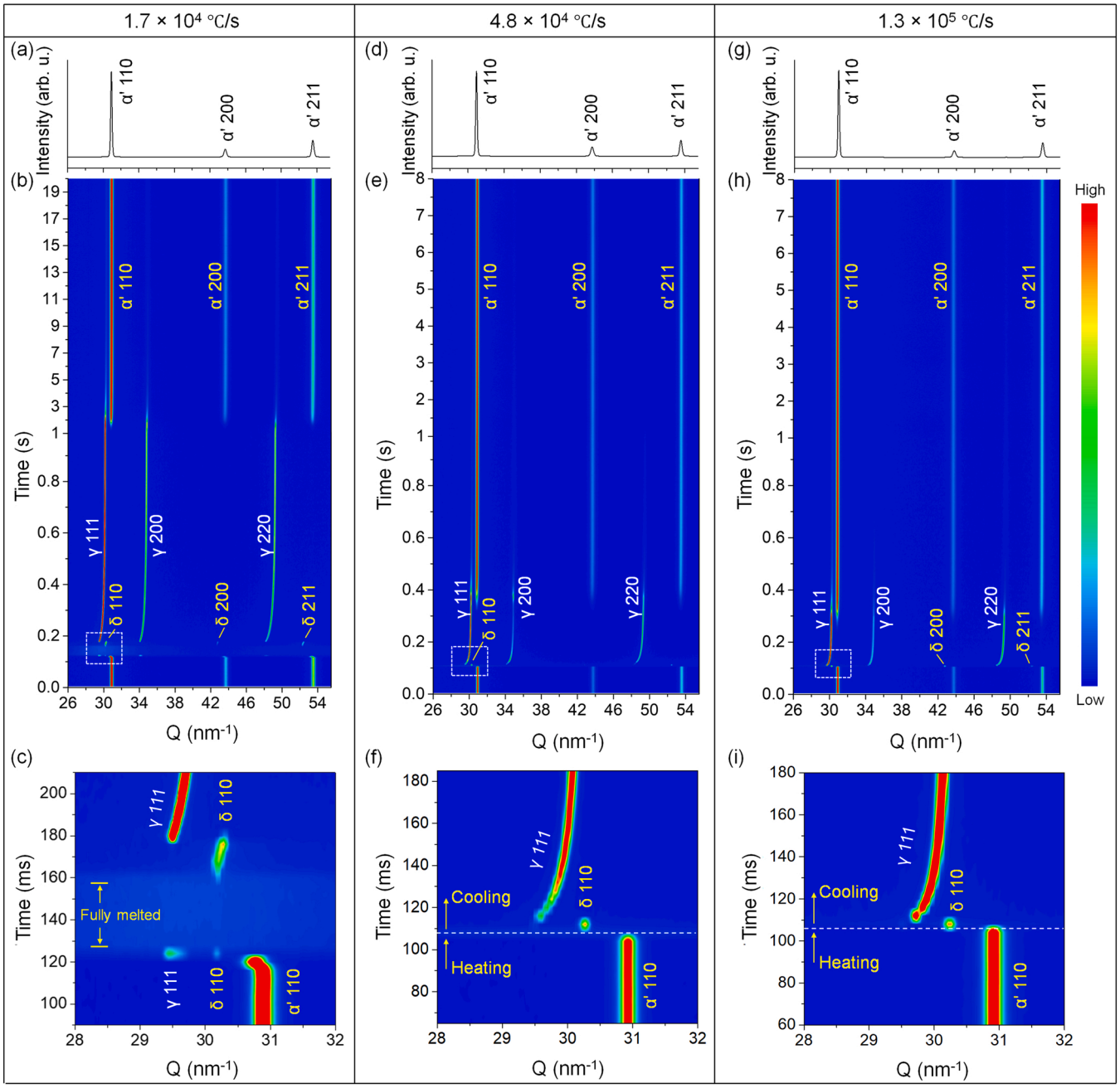

Fig. 4. Phase evolution of UW_17–4 under various cooling rates. (a) Room temperature XRD of as-solidified UW_17–4 after laser melting with a cooling rate of 1.7×10^4 °C/s. (b) XRD intensity map during laser melting from 0 to 20 s with a cooling rate of 1.7×10^4 °C/s. (c) Zoom-in view from (b) to highlight the phase transformation during the initial solidification stage. (d–f) In-situ XRD results under a cooling rate of 4.8×10^4 °C/s. (g–i) XRD results under a cooling rate of 1.3×10^5 °C/s.

came out from the liquid, as indicated by the bright spots in Fig. 5(a). Shortly afterward (0.4 s), austenite formed and consumed all the δ-ferrite, as indicated by the γ 111, γ 200, and γ 220 diffraction patterns in Fig. 5(b) and the absence of δ 110 and δ 211 diffraction spots. Martensite started to form when the temperature dropped below the Ms point, as shown in Fig. 5(c). The martensite α' 110 and α' 211 diffraction patterns appeared as uniform, continuous rings, like powder diffraction, because martensite structure is fine and rather randomly oriented. During further cooling (10 s), as shown Fig. 5(d), more austenite transformed into martensite, with the austenite diffraction rings almost vanished. When the material cooled down to room temperature (Fig. 5 (e)), only uniform, continuous martensite diffraction rings were observed, suggesting that the final material structure is fully martensitic.

Therefore, we confirmed that the developed UW_17–4 can successfully produce fully martensitic structure under the cooling rate of 1.7×10^4 °C/s.

3.3. Consistent phase formation under various cooling rates (tolerance to cooling rate variation)

To examine whether the UW_17–4 can maintain its phase transformation behavior across various cooling conditions, we conducted more in-situ laser-melting XRD experiments under the cooling rates of 4.8×10^4 °C/s and 1.3×10^5 °C/s. Together with the cooling rate 1.7×10^4 °C/s, we presented the complete phase transformation history under each condition in Fig. 4(b, e, and h), with the initial solidification

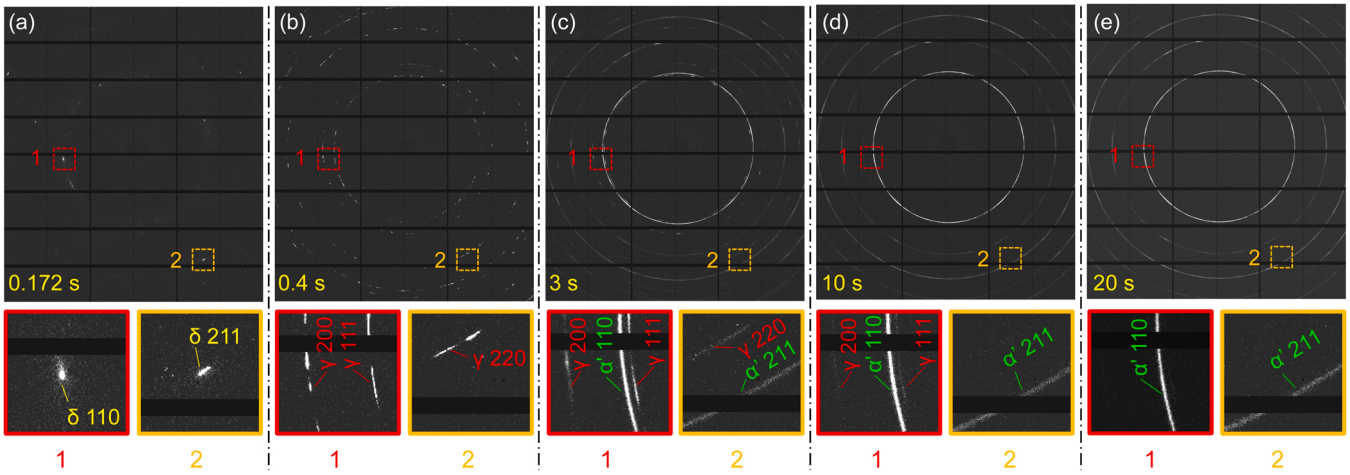

Fig. 5. Analysis of phase evolution in UW_17–4 after laser melting. The 2D diffraction patterns at different moments from Fig. 4(b) are shown in (a–e). Fig. 5 and Fig. 4(b) share the same time scale. Two signature diffraction areas 1 and 2 were marked using red and orange rectangles. The areas 1 and 2 at each moment were enlarged and displayed below the whole-field diffraction images. The horizontal and vertical black bands in the figures are no-signal zones, due to the configuration of the X-ray detector.

stage enlarged in Fig. 4(c, f, and i).

Using Fig. 4(a–c) as a reference, it can be observed that the phase transformation behaviors at higher cooling rates followed the exact same trend as the one under 1.7×10^4 °C/s. Under all conditions, δ-ferrite first solidified from the liquid, then fully transformed into austenite. The fully austenitic structure of UW_17–4 started to transform into martensite at an Ms temperature of 233 ± 21 °C (averaged from the three experiments in Fig. 4), resulting in a fully martensitic final structure, as evidenced by the room-temperature XRD patterns in Fig. 4(a, d, and g). Therefore, the UW_17–4 can reliably produce fully martensitic structure under the examined cooling rates.

Since the feasible cooling rate window for in-situ observation is limited, we conducted ex-situ laser melting and casting experiments to further study the as-solidified microstructure in UW_17–4 with extended range of cooling rates by electron backscatter diffraction (EBSD), as shown in Fig. 6. Three cooling rates on the orders of 10^2 °C/s, 10^4 °C/s, and 10^7 °C/s were accomplished by casting (arc melting), single-layer laser melting, and laser spot welding, respectively. To be noticed, the cooling rate of 2×10^4 °C/s in the single-layer laser melting sample (Fig. 6(b)) is within the cooling rate window of the in-situ experiment (Fig. 4). Hence, it serves as an orthogonal reference point for the ex-situ data. In addition, the substrate in Fig. 6(b) is a piece of UW_17–4 after condition-A solution heat treatment. During condition-A heat treatment, the material was heated up to 1038 °C (above its austenite temperature), held for 45 min, and followed by quenching. All potential δ-ferrite will transform into austenite during the long time holding at high temperature. During quenching, all austenite will transform into martensite. Hence, the substrate microstructure in Fig. 6(b) is fully martensitic and also serves as a reference point for other ex-situ experiments.

EBSD data in Fig. 6 confirm that the microstructures under the three cooling rates (10^2 °C/s, 10^4 °C/s, 10^7 °C/s) were all fully martensitic, as indicated by the image quality (IQ) maps of Fig. 6(a–c). The consistent dark netlike features in the IQ maps are signatures of martensite resulting from its poor diffraction quality caused by internal high-density lattice defects (such as dislocations and sub-grain boundaries) [37,42–44]. These features are distinct from the δ-ferrite IQ map in Fig. 1(e), where the δ-ferrite grains appear much brighter due to less lattice defects. The IQ map in Fig. 6(b) shows a slight difference in the imaging contrast, where the left half field-of-view is darker than the right half. This observation is due to a refined structure obtained under high cooling rate, as exhibited in the inversed pole figure (IPF) of Fig. 6 (b). The details of the refined structure were zoomed in and displayed in Fig. 6(d).

We demonstrate that our developed alloy, UW_17–4, consistently forms a fully martensitic final structure under a broad range of cooling rates (10^2–10^7 °C/s), with in-situ and postmortem examinations. This cooling rate range encompasses all major types of fusion-based AM technologies.

3.4. Tolerance to environmental impurity

In addition to good tolerance to cooling rates, a robust material for AM must have good resistance to environmental impurities. Environmental impurities in AM refer to the elements not within the alloy specifications. It is almost inevitable to entrain environmental impurities to the alloy during AM processing. For example, the directed energy deposition (DED) AM processes, especially the wire-based DED process [45], sometimes are performed in open environment with flowing inert gas blowing toward the laser-matter interaction area. The inert gas could easily mix with the environment air during the process.

Here, we demonstrate UW_17–4 can consistently produce a fully martensitic structure with impurity in the processing environment. To simulate environment impurities, we mixed a 20 vol% air with an 80 vol % shielding argon gas. Under this mixed-gas environment, we re-melted an exact material location for up to three times and monitored the phase transformation using in-situ XRD. The results are shown in Fig. 7. After the 3rd re-melting, the final phase structure is still fully martensitic, as evidenced by the BCC peaks in Fig. 7(g) and the complete δ–γ–α' transformation in Fig. 7(h and i). In addition, among the three re-melting experiments, we did not observe significant differences regarding phase transformation sequence and temperature, indicating a good tolerance of UW_17–4 to typical processing environmental impurities.

3.5. Structure and property of as-printed UW_17-4

To examine our developed alloy in actual AM process, we fabricated a UW_17–4 part using a laser powder bed fusion system. The final structure in the as-printed part was fully BCC structure (> 99.9 mass %), as confirmed by the synchrotron XRD data in Fig. 8(a), which contains bulk structural information from a sampling volume of 1.0 mm × 0.6 mm × 0.8 mm. Further EBSD examination revealed fully martensitic features on the IQ map of the as-printed UW_17–4 (Fig. 8 (b)), similarly to those shown in Fig. 6. Given the combined evidence from Fig. 8(a and b), we conclude that the as-printed UW_17–4 part is fully martensitic.

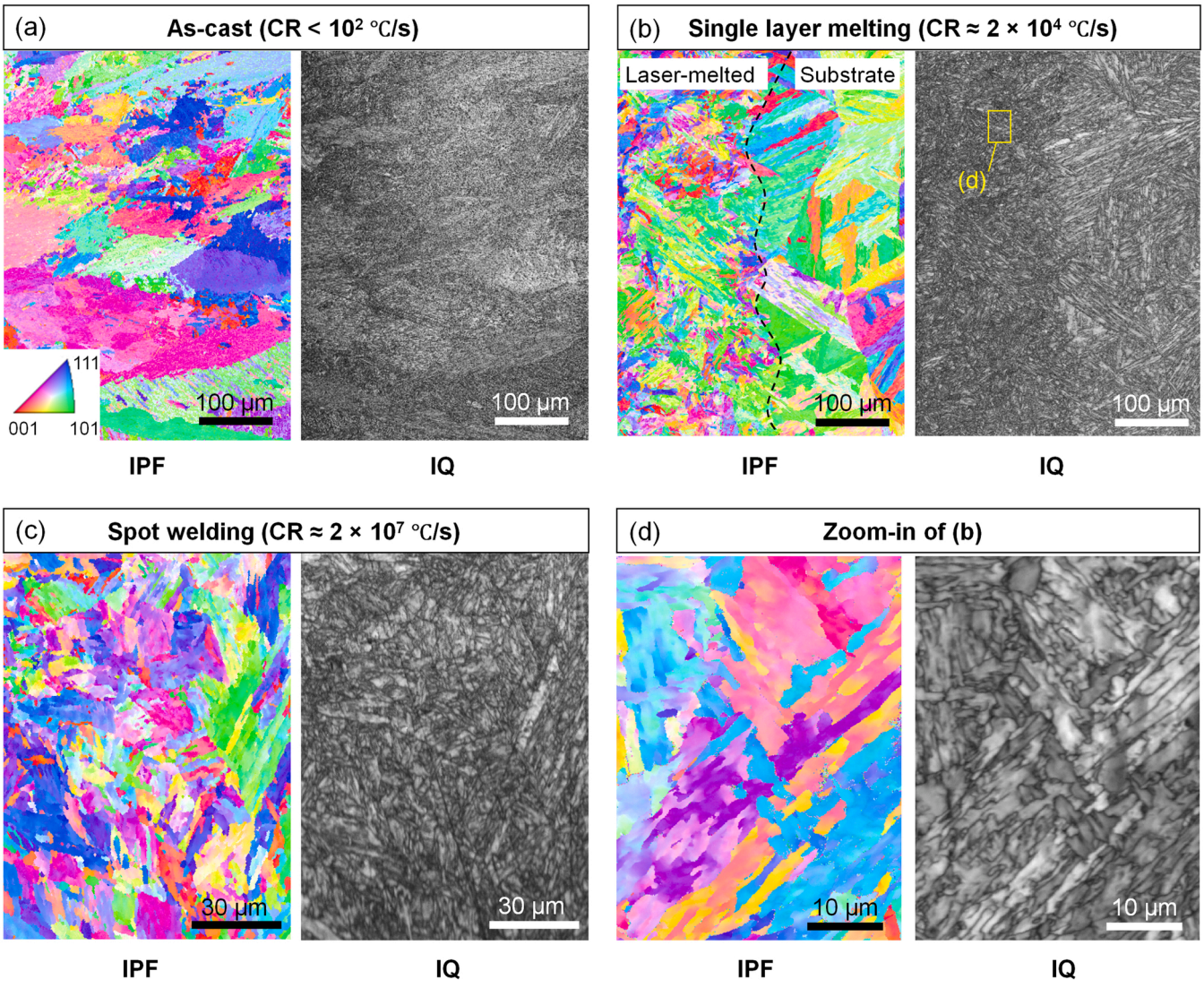

Fig. 6. Microstructure of as-solidified UW_17–4 under various cooling rates. (a) EBSD of as-cast UW_17–4 fabricated by arc-melting. The left panel is an inversed pole figure (IPF). The right panel is the corresponding image quality (IQ) map. (b) EBSD of UW_17–4 after a single-layer laser melting (transverse cross-section). The substrate is a cast, fully martensitic UW_17–4 after a solution heat treatment. (c) EBSD of UW_17–4 after laser spot welding under 156 W laser power with 1 ms laser duration (transverse cross-section). (d) EBSD of a zoom-in area from (b). The microstructures for all conditions are fully martensitic. All IPFs share the same color code, which is shown in the inset of (a).

We characterized the mechanical properties of the as-printed UW_17–4 with tensile testing. The engineering stress-strain tensile curves of the as-printed UW_17–4 are compared with their counterparts: as-printed C_17–4 and commercial wrought 17–4 after condition-A solution hear treatment (fully martensitic), with a reference point being the specification of 17–4 PH stainless steel after condition-A + H900 heat treatment (fully martensitic + precipitation hardening). The results exhibited in Fig. 8(c) demonstrate that: (1) the as-printed UW_17–4 has a yield strength of 1157 ± 23 MPa, which is over 40 % (346 MPa) higher than that of the as-printed C_17–4 (811 ± 16 MPa); (2) the yield strength of the UW_17–4 in the as-printed condition is comparable to that of the 17–4 steel specification (1170 MPa) after a precipitation hardening heat treatment.

The as-printed UW_17–4 possesses high yield strength that cannot be solely explained by UW_17–4 being fully martensitic because otherwise it would have a similar yield strength to the solution heat-treated wrought 17–4 steel (Fig. 8(c)). A probable reason for the unexpected high yield strength is the existence of copper-rich precipitates, which are a major contributor to the extra strength in precipitation-hardened 17–4 steel [28]. To test this hypothesis, we performed small-angle X-ray scattering (SAXS) measurements on as-printed UW_17–4. The SAXS data contain statistically meaningful information from a bulk specimen of 0.8 mm × 0.8 mm × 0.1 mm. The SAXS results in Fig. 9(a) unequivocally revealed a scattering feature with a nominal size of ~4 nm (orange line). This size is characteristic of the copper-rich precipitates in the 17–4 PH steel [46,47]. We further performed atom probe tomography (APT) from the same as-printed UW_17–4 sample. The APT results displaying in Fig. 9(b) validated our hypothesis that a high density of Cu-rich precipitation particles exist in the as-printed UW_17–4. It is likely that these small precipitates formed during the cyclic heating/cooling process in AM, which represents an intrinsic heat treatment. An additional characteristic length on the scale of 50 nm also showed up on the SAXS curve in Fig. 9(a), which is a good match with the metallurgical pores in the as-printed material, as exhibited by the SEM image in Fig. 9(c) and supported by the statistical analysis of pore size distributions within a representative area (Fig. 9(d)).

4. Conclusions

Informed by phase transformation dynamics, we developed a robust

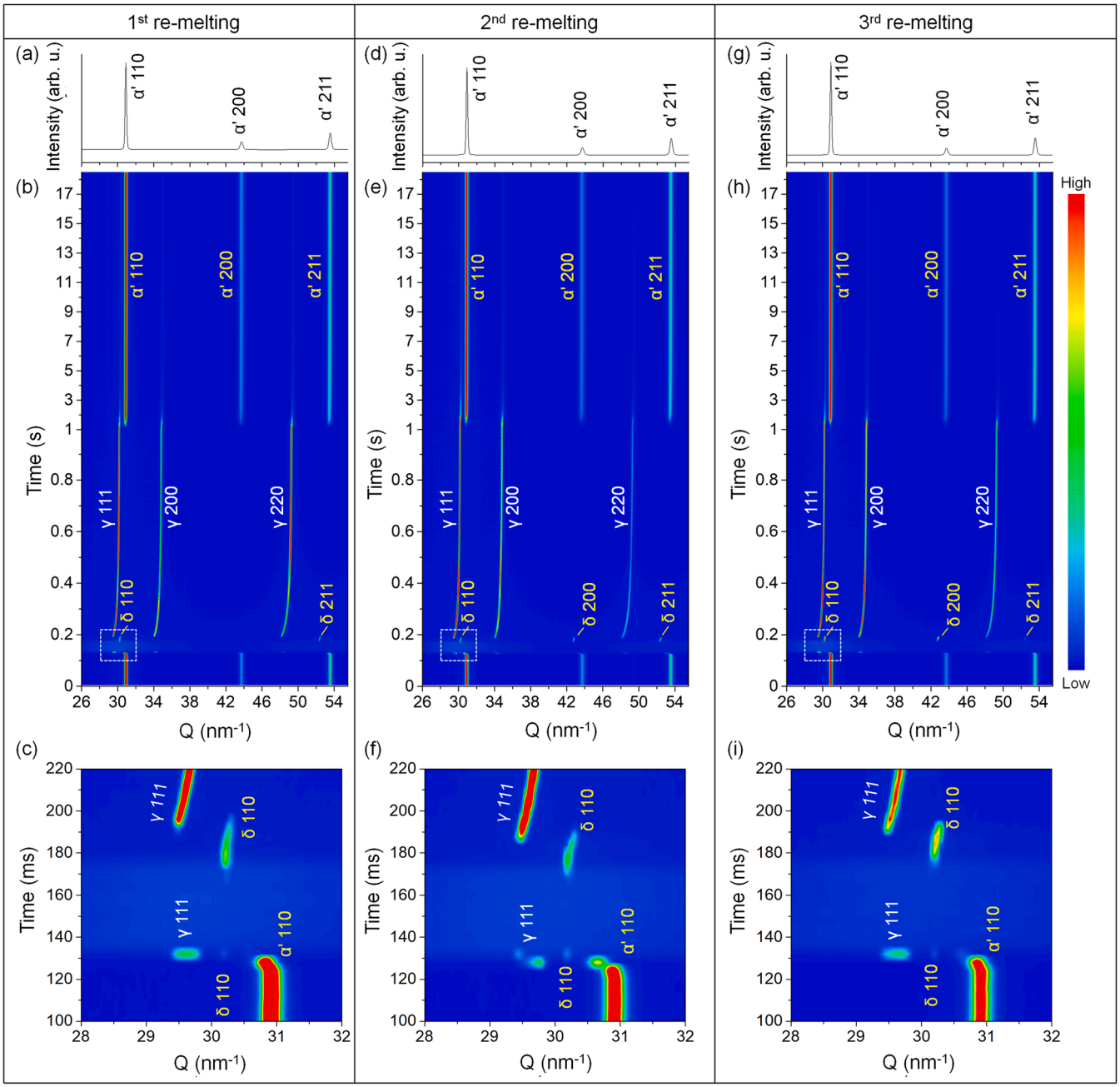

Fig. 7. Phase evolution of UW_17–4 with impurity in the environment gas. The processing environment contains 80 vol% argon as the main protection gas and 20 vol% air as an impurity. (a) Room temperature XRD of as-solidified UW_17–4 after 1st laser re-melting. (b) XRD intensity map during 1st laser re-melting from 0 s to 18.5 s (c) Zoom-in view from (b) to highlight phase transformation during the initial solidification. (d–f) XRD results of laser re-melting for the 2nd time at the same location as in (a–c). (g–i) XRD results of laser re-melting for the 3rd time at the same location as in (a–c).

martensitic 17–4 stainless steel (UW_17–4) for additive manufacturing. The alloy development strategy reported here signifies the importance of understanding phase transformation dynamics under AM conditions. Probed by in-situ high-speed high-energy high-resolution X-ray diffraction, the phase transformation dynamics of C_17–4 PH stainless steel during rapid solidification guided our development to target the initial liquid-solid phase transformation during solidification. Our alloy development strategy mitigated the formation of initial δ-ferrite phase and promoted the austenite-to-martensite transformation to achieve the desired fully martensitic phase in the final structure of the UW_17–4. We demonstrated that the developed alloy could maintain fully martensitic structure in the as-solidified state under a wide range of cooling rates (10^2–10^7 °C/s) and withstands common environment impurities. The tolerance of the material to the complex thermal and chemical environments is critical for industrial adoption to achieve reliable and consistent additively manufactured parts, regardless of the differences among AM machines, printing batches, and printing regions. The one-step fabrication of desired phases (matrix and precipitates) in the as-printed additively manufactured parts might eliminate the costly and complex post heat treatment required for phase-adjustment, which has potential to greatly improve production efficiency with reduced cost on time, energy, and labor. We expect that phase transformation dynamics guided alloy development will lead to the development of more robust, high-performance materials for the additive manufacturing industry.

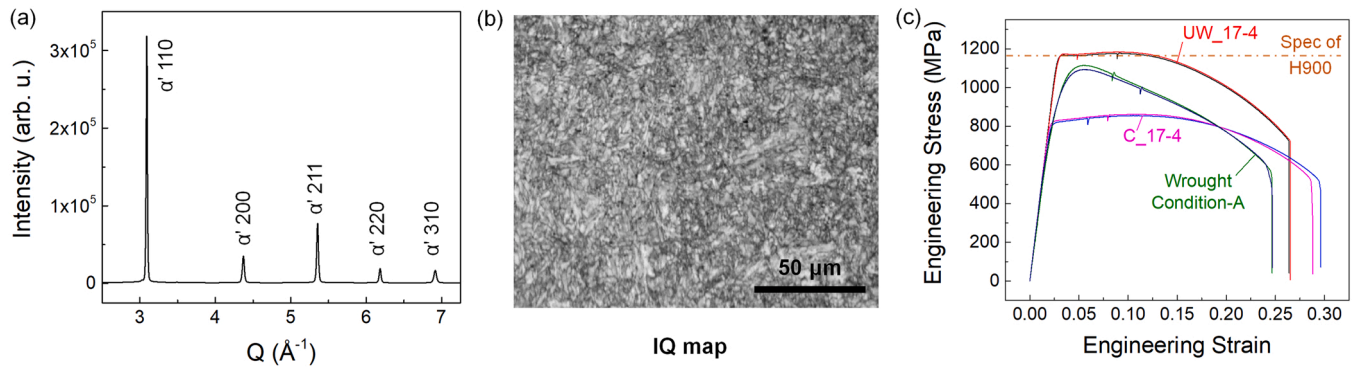

Fig. 8. Structure and property of as-printed UW_17–4. (a) High-resolution synchrotron XRD of as-printed UW_17–4. The XRD sample volume was 1.0 mm × 0.6 mm × 0.8 mm. (b) IQ map of as-printed UW_17–4 by EBSD characterization. (c) Tensile curves of the as-printed UW_17–4, as-printed C_17–4, and commercial wrought 17–4 steel after condition-A solution heat treatment (Wrought Condition-A). Two tensile curves are shown for each material. The orange line is the minimum specification of precipitation-hardened 17–4 PH stainless steel after H900 heat treatment.

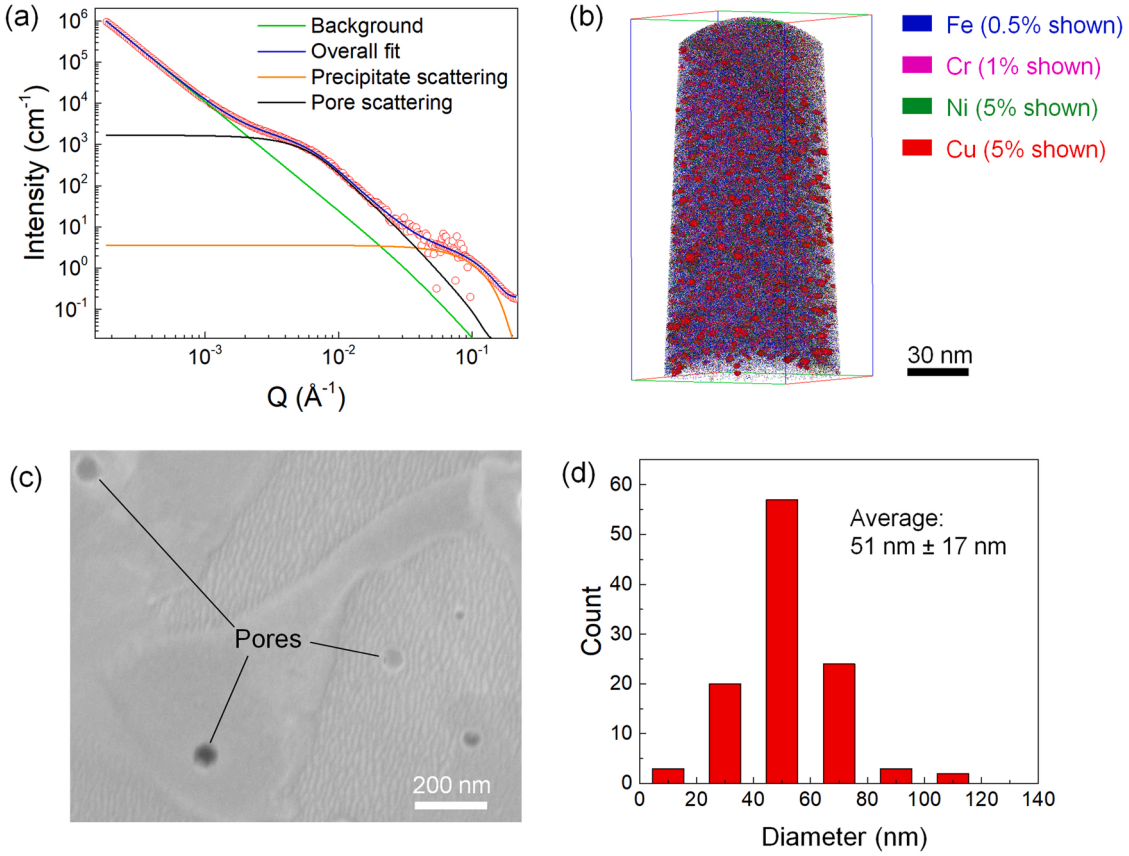

Fig. 9. Analysis of nanoprecipitates in the as-printed UW_17–4. (a) Small-angle scattering (SAXS) of as-printed UW_17–4. (b) Atom probe tomography (APT) image showing the element map of the as-printed UW_17–4. The Cu-rich precipitates have an average size of ~4 nm. (c) SEM image showing the metallurgical pores in the as-printed UW_17–4. (d) Statistics of the metallurgical pores distributing within a 21.79 μm × 14.55 μm area.

CRediT authorship contribution statement

Qilin Guo: Validation, Methodology, Investigation, Formal analysis, Data curation, Writing - original draft. **Minglei Qu:** Methodology. **Chihpin Andrew Chuang:** Resources, Methodology. **Lianghua Xiong:** Methodology, Investigation. **Ali Nabaa:** Methodology. **Zachary A. Young:** Methodology. **Yang Ren:** Resources, Methodology. **Peter Kenesei:** Methodology. **Fan Zhang:** Writing – review & editing, Validation, Supervision, Resources, Methodology, Investigation. **Lianyi Chen:** Supervision, Resources, Project administration, Methodology, Investigation, Funding acquisition, Conceptualization, Writing - original draft.

Declaration of Competing Interest

The authors declare the following financial interests/personal relationships which may be considered as potential competing interests: Wisconsin Alumni Research Foundation (WARF) has filed a patent with Lianyi Chen and Qilin Guo as inventors for the UW_17–4 alloy reported in this paper. All other authors declare they have no competing interests.

Data availability

Data will be made available on request.

Acknowledgements

We thank Dr. Jan Ilavsky for his assistance with the SAXS measurement. This work is funded by the National Science Foundation (CMMI-2011354) and University of Wisconsin-Madison Startup Fund. The authors acknowledge use of facilities and instrumentation at the UW-Madison Wisconsin Centers for Nanoscale Technology (wcnt.wisc.edu) partially supported by the NSF through the University of Wisconsin Materials Research Science and Engineering Center (DMR-1720415). This research used resources of the Advanced Photon Source, a U.S. Department of Energy (DOE) Office of Science User Facility operated for the DOE Office of Science by Argonne National laboratory under contract DE-AC02-06CH11357. Atom-probe tomography was performed at the Northwestern University Center for Atom-Probe Tomography (NUCAPT). The LEAP tomograph at NUCAPT was purchased and upgraded with grants from the NSF-MRI (DMR-0420532) and ONR-DURIP (N00014-0400798, N00014-0610539, N00014-0910781, N00014-1712870) programs. NUCAPT received support from the MRSEC program (NSF DMR-1720139) at the Materials Research Center, the SHyNE Resource (NSF ECCS-2025633), and the Initiative for Sustainability and Energy (ISEN) at Northwestern University. National Institute of Standards and Technology disclaimer: Certain commercial equipment, instruments, software or materials are identified in this paper to foster understanding. Such identification does not imply recommendation or endorsement by the Department of Commerce or the National Institute of Standards and Technology, nor does it imply that the materials or equipment identified are necessarily the best available for the purpose.

Appendix A. Supporting information

Supplementary data associated with this article can be found in the online version at doi:10.1016/j.addma.2022.103068.

References

[1] T. DebRoy, T. Mukherjee, H.L. Wei, J.W. Elmer, J.O. Milewski, Metallurgy, mechanistic models and machine learning in metal printing, Nat. Rev. Mater. 6 (2021) 48–68, https://doi.org/10.1038/s41578-020-00236-1.

[2] T.D. Ngo, A. Kashani, G. Imbalzano, K.T.Q. Nguyen, D. Hui, Additive manufacturing (3D printing): A review of materials, methods, applications and challenges, Compos. Part B Eng. 143 (2018) 172–196, https://doi.org/10.1016/j.compositesb.2018.02.012.

[3] H. Fayazfar, M. Salarian, A. Rogalsky, D. Sarker, P. Russo, V. Paserin, E. Toyserkani, A critical review of powder-based additive manufacturing of ferrous alloys: Process parameters, microstructure and mechanical properties, Mater. Des. 144 (2018) 98–128, https://doi.org/10.1016/j.matdes.2018.02.018.

[4] M. Qian, W. Xu, M. Brandt, H.P. Tang, Additive manufacturing and postprocessing of Ti-6Al-4V for superior mechanical properties, MRS Bull. 41 (2016) 775–784, https://doi.org/10.1557/mrs.2016.215.

[5] W.M. Tucho, P. Cuvillier, A. Sjolyst-Kverneland, V. Hansen, Microstructure and hardness studies of Inconel 718 manufactured by selective laser melting before and after solution heat treatment, Mater. Sci. Eng. A 689 (2017) 220–232, https://doi.org/10.1016/j.msea.2017.02.062.

[6] K. Amato, Comparison of microstructures and properties for a Ni-base superalloy (Alloy 625) fabricated by electron beam melting, J. Mater. Sci. Res 1 (2012) 3, https://doi.org/10.5539/jmsr.v1n2p3.

[7] M. Alnajjar, F. Christien, C. Bosch, K. Wolski, A.D. Fortes, M. Telling, In-situ neutron diffraction study of wrought and selective laser melted maraging stainless steels, Mater. Charact. 172 (2021), 110840, https://doi.org/10.1016/j.matchar.2020.110840.

[8] A.J. Shahani, A.J. Clarke, Processing metallic materials far from equilibrium, MRS Bull. 45 (2020) 906–909, https://doi.org/10.1557/mrs.2020.269.

[9] X. Tan, Y. Kok, Y.J. Tan, M. Descoins, D. Mangelinck, S.B. Tor, K.F. Leong, C. K. Chua, Graded microstructure and mechanical properties of additive manufactured Ti–6Al–4V via electron beam melting, Acta Mater. 97 (2015) 1–16, https://doi.org/10.1016/j.actamat.2015.06.036.

[10] P. Kürnsteiner, M.B. Wilms, A. Weisheit, B. Gault, E.A. Jägle, D. Raabe, High-strength Damascus steel by additive manufacturing, Nature 582 (2020) 515–519, https://doi.org/10.1038/s41586-020-2409-3.

[11] Y. Kok, X.P. Tan, P. Wang, M.L.S. Nai, N.H. Loh, E. Liu, S.B. Tor, Anisotropy and heterogeneity of microstructure and mechanical properties in metal additive manufacturing: A critical review, Mater. Des. 139 (2018) 565–586, https://doi.org/10.1016/j.matdes.2017.11.021.

[12] L. Zai, C. Zhang, Y. Wang, W. Guo, D. Wellmann, X. Tong, Y. Tian, Laser powder bed fusion of precipitation-hardened martensitic stainless steels: a review, Metals 10 (2020) 255, https://doi.org/10.3390/met10020255.

[13] C.N.N. Hsiao, C.S.S. Chiou, J.R.R. Yang, Aging reactions in a 17-4 PH stainless steel, Mater. Chem. Phys. 74 (2002) 134–142, https://doi.org/10.1016/S0254-0584(01)00460-6.

[14] E.A. Lass, F. Zhang, C.E. Campbell, Nitrogen effects in additively manufactured martensitic stainless steels: conventional thermal processing and comparison with wrought, Metall. Mater. Trans. A 51 (2020) 2318–2332, https://doi.org/10.1007/s11661-020-05703-6.

[15] A.A. Adeyemi, E.T. Akinlabi, R.M. Mahamood, K.O. Sanusi, S. Pityana, M. Tlotleng, Influence of laser power on microstructure of laser metal deposited 17-4 PH stainless steel, IOP Conf. Ser. Mater. Sci. Eng. 225 (2017), 012028, https://doi.org/10.1088/1757-899X/225/1/012028.

[16] M. Alnajjar, F. Christien, K. Wolski, C. Bosch, Evidence of austenite by-passing in a stainless steel obtained from laser melting additive manufacturing, Addit. Manuf. 25 (2019) 187–195, https://doi.org/10.1016/j.addma.2018.11.004.

[17] L. Facchini, N. Vicente, I. Lonardelli, E. Magalini, P. Robotti, A. Molinari, N. Vicente Jr, I. Lonardelli, E. Magalini, P. Robotti, A. Molinari, Metastable austenite in 17-4 precipitation-hardening stainless steel produced by selective laser melting, Adv. Eng. Mater. 12 (2010) 184–188, https://doi.org/10.1002/adem.200900259.

[18] L.E. Murr, E. Martinez, J. Hernandez, S. Collins, K.N. Amato, S.M. Gaytan, P. W. Shindo, Microstructures and properties of 17-4 PH stainless steel fabricated by selective laser melting, J. Mater. Res. Technol. 1 (2012) 167–177, https://doi.org/10.1016/S2238-7854(12)70029-7.

[19] P. Leo, M. Cabibbo, A. Del Prete, S. Giganto, S. Martínez-Pellitero, J. Barreiro, Laser defocusing effect on the microstructure and defects of 17-4PH parts additively manufactured by slm at a low energy input, Metals 11 (2021) 588, https://doi.org/10.3390/met11040588.

[20] T.-H. Hsu, P.-C. Huang, M.-Y. Lee, K.-C. Chang, C.-C. Lee, M.-Y. Li, C.-P. Chen, K.-K. Jen, A.-C. Yeh, Effect of processing parameters on the fractions of martensite in 17-4 PH stainless steel fabricated by selective laser melting, J. Alloy. Compd. 859 (2021), 157758, https://doi.org/10.1016/j.jallcom.2020.157758.

[21] I. Mathoho, E.T. Akinlabi, N. Arthur, M. Tlotleng, Impact of DED process parameters on the metallurgical characteristics of 17-4 PH SS deposited using DED, CIRP J. Manuf. Sci. Technol. 31 (2020) 450–458, https://doi.org/10.1016/j.cirpj.2020.07.007.

[22] A. Caballero, J. Ding, S. Ganguly, S. Williams, Wire + Arc additive manufacture of 17-4 PH stainless steel: effect of different processing conditions on microstructure, hardness, and tensile strength, J. Mater. Process. Technol. 268 (2019) 54–62, https://doi.org/10.1016/j.jmatprotec.2019.01.007.

[23] F.S.H.B. Freeman, A. Lincoln, J. Sharp, A. Lambourne, I. Todd, Exploiting thermal strain to achieve an in-situ magnetically graded material, Mater. Des. 161 (2019) 14–21, https://doi.org/10.1016/j.matdes.2018.11.011.

[24] F. Zhang, M.R. Stoudt, S. Hammadi, C.E. Campbell, E.A. Lass, M.E. Williams, How austenitic is a martensitic steel produced by laser powder bed fusion? A cautionary tale, Metals 11 (2021) 1924, https://doi.org/10.3390/met11121924.

[25] M.S. Moyle, N. Haghdadi, X.Z. Liao, S.P. Ringer, S. Primig, On the microstructure and texture evolution in 17-4 PH stainless steel during laser powder bed fusion: towards textural design, J. Mater. Sci. Technol. 117 (2022) 183–195, https://doi.org/10.1016/j.jmst.2021.12.015.

[26] H.K. Rafi, D. Pal, N. Patil, T.L. Starr, B.E. Stucker, Microstructure and mechanical behavior of 17-4 precipitation hardenable steel processed by selective laser melting, J. Mater. Eng. Perform. 23 (2014) 4421–4428, https://doi.org/10.1007/s11665-014-1226-y.

[27] X. Wang, G. Wang, T. Shi, Y. Wang, Tensile mechanical behavior and spall response of a selective laser melted 17-4 PH stainless steel, Metall. Mater. Trans. A 52 (2021) 2369–2388, https://doi.org/10.1007/s11661-021-06229-1.

[28] A. Yadollahi, N. Shamsaei, S.M. Thompson, A. Elwany, L. Bian, Effects of building orientation and heat treatment on fatigue behavior of selective laser melted 17-4 PH stainless steel, Int. J. Fatigue 94 (2017) 218–235, https://doi.org/10.1016/j.ijfatigue.2016.03.014.

[29] C. Zhao, K. Fezzaa, R.W. Cunningham, H. Wen, F. De Carlo, L. Chen, A.D. Rollett, T. Sun, Real-time monitoring of laser powder bed fusion process using high-speed X-ray imaging and diffraction, Sci. Rep. 7 (2017) 3602, https://doi.org/10.1038/s41598-017-03761-2.

[30] S.A. Oh, R.E. Lim, J.W. Aroh, A.C. Chuang, B.J. Gould, J.V. Bernier, N. Parab, T. Sun, R.M. Suter, A.D. Rollett, Microscale observation via high-speed X-ray diffraction of alloy 718 during in situ laser melting, JOM 73 (2021) 212–222, https://doi.org/10.1007/s11837-020-04481-1.

[31] S. Karnati, I. Axelsen, F.F. Liou, J.W. Newkirk, Investigation of tensile properties of bulk and SLM fabricated 304L stainless steel using various gage length specimens, in: Proceedings of the Twenty Seventh Annu. Int. Solid Free. Fabr. Symp. Addit. Manuf. Conf., 2016, 592–604.

[32] F. Zhang, J. Ilavsky, G.G. Long, J.P.G. Quintana, A.J. Allen, P.R. Jemian, Glassy carbon as an absolute intensity calibration standard for small-angle scattering, Metall. Mater. Trans. A 41 (2010) 1151–1158, https://doi.org/10.1007/s11661-009-9950-x.

[33] J. Ilavsky, F. Zhang, R.N. Andrews, I. Kuzmenko, P.R. Jemian, L.E. Levine, A. J. Allen, Development of combined microstructure and structure characterization

facility for in situ and operando studies at the advanced photon source, J. Appl. Crystallogr. 51 (2018) 867–882, https://doi.org/10.1107/S160057671800643X.
[34] F. Zhang, L.E. Levine, A.J. Allen, M.R. Stoudt, G. Lindwall, E.A. Lass, M. E. Williams, Y. Idell, C.E. Campbell, Effect of heat treatment on the microstructural evolution of a nickel-based superalloy additive-manufactured by laser powder bed fusion, Acta Mater. 152 (2018) 200–214, https://doi.org/10.1016/j.actamat.2018.03.017.
[35] J. Ilavsky, P.R. Jemian, Irena: tool suite for modeling and analysis of small-angle scattering, J. Appl. Crystallogr. 42 (2009) 347–353, https://doi.org/10.1107/S0021889809002222.
[36] F. Villaret, X. Boulnat, P. Aubry, J. Zollinger, D. Fabrègue, Y. de Carlan, Modelling of delta ferrite to austenite phase transformation kinetics in martensitic steels: application to rapid cooling in additive manufacturing, Materialia 18 (2021), 101157, https://doi.org/10.1016/j.mtla.2021.101157.
[37] S. Vunnam, A. Saboo, C. Sudbrack, T.L. Starr, Effect of powder chemical composition on the as-built microstructure of 17-4 PH stainless steel processed by selective laser melting, Addit. Manuf. 30 (2019), 100876, https://doi.org/10.1016/j.addma.2019.100876.
[38] S. Sabooni, A. Chabok, S.C. Feng, H. Blaauw, T.C. Pijper, H.J. Yang, Y.T. Pei, Laser powder bed fusion of 17–4 PH stainless steel: a comparative study on the effect of heat treatment on the microstructure evolution and mechanical properties, Addit. Manuf. 46 (2021), 102176, https://doi.org/10.1016/j.addma.2021.102176.
[39] J. Wang, P.J. van der Wolk, S. van der Zwaag, Determination of martensite start temperature in engineering steels part I. Empirical relations describing the effect of steel chemistry, Mater. Trans. JIM 41 (2000) 761–768, https://doi.org/10.2320/matertrans1989.41.761.
[40] C. Capdevila, F.G. Caballero, C.G. de Andrés, Determination of Ms temperature in steels: a bayesian neural network model, ISIJ Int. 42 (2002) 894–902, https://doi.org/10.2355/isijinternational.42.894.
[41] S.M.H. Hojjatzadeh, N.D. Parab, Q. Guo, M. Qu, L. Xiong, C. Zhao, L.I. Escano, K. Fezzaa, W. Everhart, T. Sun, L. Chen, Direct observation of pore formation mechanisms during LPBF additive manufacturing process and high energy density laser welding, Int. J. Mach. Tools Manuf. 153 (2020), 103555, https://doi.org/10.1016/j.ijmachtools.2020.103555.
[42] L. Ryde, Application of EBSD to analysis of microstructures in commercial steels, Mater. Sci. Technol. 22 (2006) 1297–1306, https://doi.org/10.1179/174328406×130948.
[43] J. WU, P.J. Wray, C.I. GARCIA, M. HUA, A.J. Deardo, Image quality analysis: a new method of characterizing microstructures, ISIJ Int. 45 (2005) 254–262, https://doi.org/10.2355/isijinternational.45.254.
[44] S. Zaefferer, J. Ohlert, W. Bleck, A study of microstructure, transformation mechanisms and correlation between microstructure and mechanical properties of a low alloyed TRIP steel, Acta Mater. 52 (2004) 2765–2778, https://doi.org/10.1016/j.actamat.2004.02.044.
[45] M. Akbari, R. Kovacevic, An investigation on mechanical and microstructural properties of 316LSi parts fabricated by a robotized laser/wire direct metal deposition system, Addit. Manuf. 23 (2018) 487–497, https://doi.org/10.1016/j.addma.2018.08.031.
[46] G. Yeli, M.A. Auger, K. Wilford, G.D.W.W. Smith, P.A.J.J. Bagot, M.P. Moody, Sequential nucleation of phases in a 17-4PH steel: microstructural characterisation and mechanical properties, Acta Mater. 125 (2017) 38–49, https://doi.org/10.1016/j.actamat.2016.11.052.
[47] Y. Sun, R.J. Hebert, M. Aindow, Effect of heat treatments on microstructural evolution of additively manufactured and wrought 17-4PH stainless steel, Mater. Des. 156 (2018) 429–440, https://doi.org/10.1016/j.matdes.2018.07.015.
[48] J.W. Elmer, T.A. Palmer, E.D. Specht, Direct observations of sigma phase formation in duplex stainless steels using in-situ synchrotron X-ray diffraction, Metall Mater Trans A 38 (2007) 464–475, https://doi.org/10.1007/s11661-006-9076-3.
[49] S.A. Oh, R.E. Lim, J.W. Aroh, A.C. Chuang, B.J. Gould, J.V. Bernier, N. Parab, T. Sun, R.M. Suter, A.D. Rollett, Microscale observation via high-speed X-ray diffraction of alloy 718 during in situ laser melting, JOM 73 (2021) 212–222, https://doi.org/10.1007/s11837-020-04481-1.